The Astrophysical Journal, 996:79 (15pp), 2026 January 1 https://doi.org/10.3847/1538-4357/ae1efa

UVOIR Spectrum, X-Ray Emission, and Proper Motion of the Isolated Neutron Star RX J2143.0+0654*

George G. Pavlov[1], Vadim Abramkin[2], and B. Posselt[3,1]
[1] Department of Astronomy and Astrophysics, The Pennsylvania State University, 525 Davey Lab, University Park, PA 16802, USA; ggp1@psu.edu
[2] Independent Researcher
[3] Oxford Astrophysics, University of Oxford, Denys Wilkinson Building, Keble Road, Oxford OX1 3RH, UK
Received 2025 September 12; revised 2025 November 5; accepted 2025 November 9; published 2025 December 29

Abstract

We observed the isolated neutron star (NS) RX J2143.0+0654 with the Hubble Space Telescope (HST) in the UVOIR wavelength range (0.14–1.7 μm). The UV part is consistent with a Rayleigh–Jeans tail of a thermal spectrum, $f_\nu \propto \nu^2$, while a power-law spectrum, $f_\nu \propto \nu^\alpha$ with $\alpha \sim -0.8$, dominates in the near-IR–optical. A joint fit of the UVOIR and contemporaneous X-ray spectra with a two-component blackbody with possible absorption features + power-law optical spectrum yields the following temperature and apparent radius of the colder component (which gives the main contribution in the UV): $kT_{\rm cold} \approx 45$ eV and $R_{\rm cold} \approx 6 d_{260}$ km, where d_{260} is the distance in units of 260 pc. The temperature and radius of the hotter component, $kT_{\rm hot} \approx 106$ eV and $R_{\rm hot} \approx 1.5 d_{260}$ km; the parameters of an absorption feature at 0.74 keV; and the properties of X-ray pulsations are the same as found in previous X-ray observations. In the near-IR images, the NS is possibly surrounded by extended emission with a characteristic size of $\sim 2''$ and flux densities of about 1.7 and 0.9 μJy at 1.54 and 1.15 μm, respectively. Comparison with a previous HST observation in the optical 14 yr ago shows a proper motion $\mu \approx 6$ mas yr^{-1}, which corresponds to a small transverse velocity of $7 d_{260}$ km s^{-1}. It is consistent with the hypothesis that the NS was born in the vicinity of the solar system about 0.5 Myr ago.

Unified Astronomy Thesaurus concepts: Neutron stars (1108)

1. Introduction

1.1. Properties of XTINSs

A family of seven nearby ($d \lesssim 1$ kpc) neutron stars (NSs), very different from the commonly known rotation-powered pulsars (RPPs), was discovered in the 1990s with the X-ray observatory ROSAT (see F. Haberl 2007 and D. L. Kaplan & M. H. van Kerkwijk 2009a for reviews). These young ($\lesssim$1 Myr), slowly rotating ($P = 3$–12 s) NSs show predominantly thermal X-ray spectra with temperatures $kT \sim 50$–100 eV. Unlike the RPPs, their X-ray luminosities, $L_{\rm X} \sim 10^{30.8}$–$10^{32.5}$ erg s^{-1}, are higher than the NS spin-down energy loss rates, $\dot{E} \sim 10^{29.4}$–$10^{30.7}$ erg s^{-1}, and, unlike RPPs, they do not show easily detectable nonthermal X-ray, radio, or γ-ray emission. Their surface magnetic fields $B \sim 10^{13}$ G, as well as positions in the period—period derivative (P-$\dot{P}$) diagram, place them between ordinary RPPs and magnetars. Various names and abbreviations have been suggested for this NS group (INS, RQINS, XTINS, XDINS, Mag7, etc.). We will call them *X-ray thermal isolated NSs* (XTINSs). Although only seven XTINSs have been firmly detected (and a few candidates found with eROSITA; A. M. Pires et al. 2022; J. Kurpas et al. 2024), population studies show that such NSs, whose soft X-ray emission is absorbed in the interstellar medium (ISM) at large distances, may represent nearly half of the local NS population (e.g., B. Posselt et al. 2008).

Fits of the X-ray spectra of XTINSs with blackbody (BB) models made it possible to estimate their surface temperatures T and radius-to-distance ratios R/d (F. Haberl 2007; D. L. Kaplan & M. H. van Kerkwijk 2009a). Some XTINSs have possibly shown variations of X-ray emission (F. Haberl et al. 2006; A. M. Pires et al. 2019; A. Mancini Pires et al. 2023), but only for RX J0720.4–3125 are there enough data to test possible explanations (e.g., M. M. Hohle et al. 2012). According to M. H. van Kerkwijk et al. (2007), the variations cannot be explained by the previously proposed NS precession, while episodes of accretion of circumstellar bodies, e.g., asteroids, remain a viable interpretation.

Based on the X-ray results, it was expected that the UV–optical (UVO) spectra of XTINSs are simply Rayleigh–Jeans (R-J) tails of the thermal X-ray spectra. However, Hubble Space Telescope (HST) observations of XTINSs showed a more complicated picture. For instance, although the UVO spectrum of the brightest of these objects, RX J1856.5–3754 (hereafter J1856), has an expected slope, $f_\nu \propto \nu^2$, the UVO flux density f_ν is a factor of 7 above the extrapolation of the X-ray BB spectrum into this frequency range (e.g., M. H. van Kerkwijk & S. R. Kulkarni 2001). Also seen in other XTINSs, such *optical excess* could be explained by a model in which X-rays come from a smaller, hotter area of the NS surface, created by anisotropic heat transfer in the strong magnetic field, while the bulk of the NS surface is responsible for the UVO emission (e.g., T. M. Braje & R. W. Romani 2002). An alternative explanation is that the optical excess is due to the difference of the assumed BB emission from those of actual NS atmospheres or solid surfaces (G. G. Pavlov et al. 1996; J. F. Pérez-Azorín et al. 2006; W. C. G. Ho et al. 2007).

* Based on observations made with the NASA/ESA Hubble Space Telescope, obtained at the Space Telescope Science Institute, which is operated by the Association of Universities for Research in Astronomy, Inc., under NASA contract NAS 5-26555. These observations are associated with program #17476.

From HST observations of five other XTINSs in two bands, 1380–1570 and 4000–5600 Å, D. L. Kaplan et al. (2011, hereafter K+11) found that not only were the flux density values above the continuation of the X-ray BB into the UVO range, but also the spectral slopes were inconsistent with an R-J spectrum for four of the five XTINSs. If one naively connects the two spectral points with a straight line in the $\log\nu$–$\log f_\nu$ plane (i.e., assume $f_\nu \propto \nu^\alpha$), then the slope varied from $\alpha = 1.63 \pm 0.14$ to $\alpha = 0.53 \pm 0.08$ instead of $\alpha = 2$ for the R-J spectrum. The reason for this unexpected behavior remains unknown.

K+11 discussed hypothetical explanations, such as nonthermal emission of relativistic electrons or resonant scattering of thermal photons in the NS magnetosphere. Ü. Ertan et al. (2017) suggested that the optical emission is produced in an inner rim of a fallback disk heated by the X-ray irradiation and magnetic stresses. Since different models predict different spectra, a comparison with observed spectra could allow one to choose the right model, but it is impossible with just two spectral points available. Obviously, more spectral points in a broader wavelength range are required in order to understand the UVO spectra of XTINSs and their connection to the X-ray spectra.

The only existing HST observation of an XTINS in a near-IR (NIR) band brought another surprise. An HST observation of RX J0806.4–4123 (hereafter J0806) in $\lambda = 1.4$–$1.7\ \mu$m not only showed a factor of 500 (!) excess over the X-ray BB extrapolation, it also resolved its *extended component*, with a size of about 1″ and a $\gtrsim$50% contribution to the total flux in this band (B. Posselt et al. 2018). These authors concluded that the extended NIR emission could be the first NIR-only pulsar wind nebula (PWN) or the first resolved fallback disk around an isolated NS. It is, of course, very interesting to observe other XTINSs at (N)IR wavelengths to see how common this phenomenon is.

1.2. Previous Observations of RX J2143.0+0654

Of the five XTINSs observed by K+11 in two HST bands (HST program #11654), a particularly strong discrepancy between the observed UVO spectral slope and the R-J slope was found for RX J2143.0+0654 (hereafter J2143), also known as RBS 1774. Therefore, we chose this object for a more detailed investigation of an XTINS UV–optical–IR (UVOIR) spectrum with the goal to understand the origin of the UVOIR emission from these puzzling objects.

J2143 was discovered with the ROSAT X-ray observatory (L. Zampieri et al. 2001). Observations with the European Photon Imaging Camera (EPIC) on board the XMM-Newton X-ray observatory allowed S. Zane et al. (2005) to detect pulsations with a period $P = 9.437$ s and a pulsed fraction with a semiamplitude of 3.6% ± 0.6%. Fitting the spectrum with a BB continuum plus a Gaussian absorption line, these authors estimated a BB temperature $kT = 104.0 \pm 0.4$ eV and an unabsorbed flux $F^{\rm unabs}_{0.2-2\,{\rm keV}} \approx 5.2 \times 10^{-12}\,{\rm erg\,cm^{-2}\,s^{-1}}$. They also estimated the magnetic field, $B \sim 1.4 \times 10^{14}$ G, assuming that the absorption feature at about 0.7 keV is due to proton cyclotron absorption. Using data from the Reflection Grating Spectrometer (RGS), M. Cropper et al. (2007) suggested an additional absorption feature at 0.4 keV in J2143's spectrum.

D. L. Kaplan & M. H. van Kerkwijk (2009b) analyzed a larger set of XMM-Newton EPIC data and found spectral properties similar to those reported by S. Zane et al. (2005) and M. Cropper et al. (2007), including possible spectral features at 0.75 and 0.4 keV. These authors estimated the period derivative, consistent with $B \sim 2 \times 10^{13}$ G, to be much lower than that estimated by S. Zane et al. (2005).

A. D. Schwope et al. (2009) found another spectral model, two BBs with $kT_{\rm hot} \approx 104$ eV and $kT_{\rm cold} \approx 40$ eV, which marginally fits the EPIC + RGS data. Finally, from the analysis of several EPIC observations plus deep (210 ks) SRG/eROSITA observations, A. Mancini Pires et al. (2023) suggested a model that consists of two BBs with $kT_{\rm hot} = 107 \pm 3$ eV, $kT_{\rm cold} \approx 43$ eV, and three spectral features centered at 0.39, 0.55, and 0.74 keV. These authors also reported a decrease in the pulsed fraction to 2.5%.

S. Bogdanov & W. C. G. Ho (2024) presented a thorough timing analysis of XMM-Newton, Chandra, and NICER observations of J2143 in 2004–2023. Their timing solution gives a complicated pulse shape with three peaks per period, whose positions depend on photon energy. The measured period derivative $\dot{P} = (4.145 \pm 0.005) \times 10^{-14}\,{\rm s\,s^{-1}}$ corresponds to $\dot{E} = 2.0 \times 10^{30}\ {\rm erg\,s^{-1}}$, $B \sim 2.0 \times 10^{13}$ G, and $\tau_c \sim 3.6$ Myr.

Faint optical emission from this NS ($m_B \sim 27$) was detected with the Very Large Telescope (VLT; S. Zane et al. 2008) and the Large Binocular Telescope (A. D. Schwope et al. 2009), with photometry results discrepant by half a magnitude, which might suggest an optical variability. B. Posselt et al. (2009) found a limit of $H > 22.0$ mag ($f_\nu < 1.55\ \mu$Jy at $1.6\ \mu$m) in a VLT observation.

The most precise measurements in the UVO range have been obtained with the HST by K+11: $f_\nu = 80 \pm 5$ nJy at 4709 Å (Advanced Camera for Surveys; ACS/ Wide Field Channel; WFC F475W filter) and $f_\nu = 94 \pm 7$ nJy at 1517 Å (ACS/Solar-Blind Channel; SBC F140LP filter); the latter value is corrected to account for the recent update on SBC sensitivity (R. J. Avila et al. 2019).

Exceeding the X-ray BB extrapolation by at least a factor of 50, J2143 has the highest optical excess among all known XTINSs. For a plausible optical extinction, $A_V = 0.12$, the dereddened flux densities are $f_\nu = 95 \pm 6$ and 124 ± 8 nJy at pivot wavelengths of 4747 and 1519 Å, respectively. They can be connected by a power law (PL) $f_\nu \propto \nu^\alpha$, $\alpha = 0.23 \pm 0.08$.

A source spectrum of an unknown shape cannot be inferred from only two observational points. Therefore, we carried out new HST observations that cover the UVOIR range with five broad filters (HST program #17476; G. G. Pavlov et al. 2023). To investigate the connection of the UVOIR spectrum with the X-ray spectrum, we also requested a contemporaneous target-of-opportunity observation with the XMM-Newton observatory, which was needed to evaluate the effects of possible long-term X-ray variability on the multiwavelength properties of the target. The results of these observations are presented below.

2. Observations and Data Reduction

2.1. HST Observations

We observed J2143 on 2024 May 16–June 30 in five spectral bands (eight HST orbits; see Table 1[4]). To check for variability and measure the proper motion, we repeated the observations in the far-UV (FUV) F140LP and optical F475W

[4] See https://www.stsci.edu/hst/phase2-public/17476.pdf for technical details.

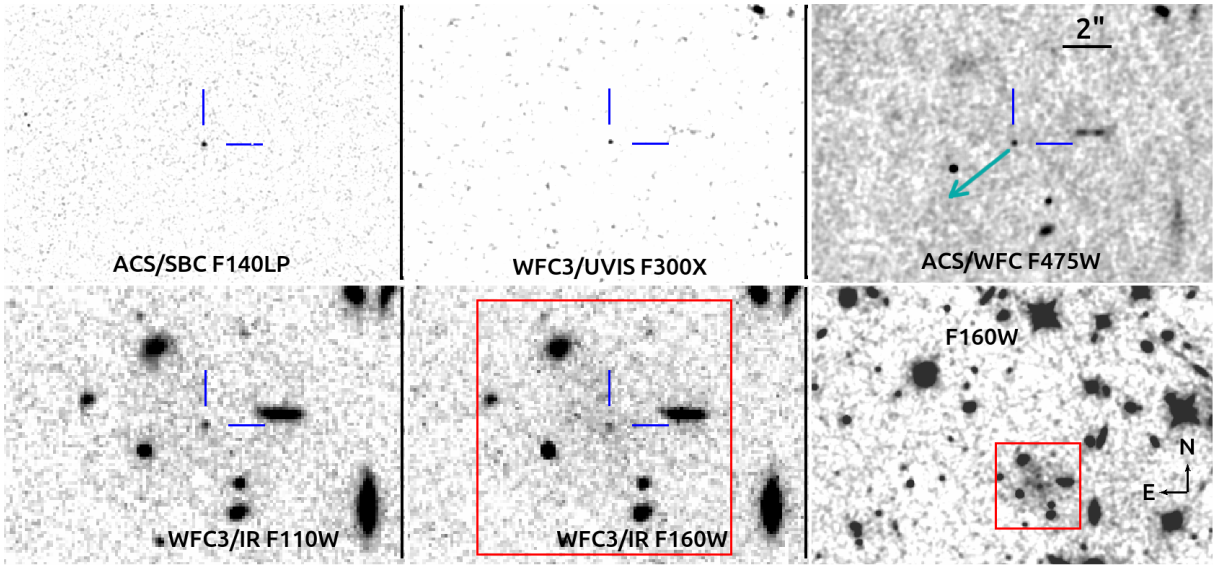

Figure 1. Images of the J2143 field, observed in five HST filters; north is up, east is left. The position of the pulsar is indicated by blue marks. Except for the bottom right, the images are of the same angular size, $\approx 16'' \times 11''$. To illustrate the enhanced emission near the location of the pulsar, the bottom right image shows a zoom-out of the WFC3/IR F160W image in the bottom middle panel, with the red box marking the same sky area. The F475W (top right) image also shows the (dark cyan) proper-motion vector (see Section 3.5).

Table 1
HST Observations of J2143

Start Time (UT)	Instrument	Filter	λ_{piv} (Å)	W_{eff} (Å)	Exposure (s)
2024-05-16 19:40:28	WFC3/UVIS2	F300X	2813	747	4926
2024-05-17 06:43:53	ACS/SBC	F140LP	1519	259	2610
2024-05-18 20:39:42	ACS/WFC	F475W	4747	1272	4184
2024-06-18 16:14:02	ACS/SBC	F140LP	1519	259	2488
2024-06-30 19:05:54	WFC3/IR	F160W	15369	2750	2497
2024-06-30 19:18:04	WFC3/IR	F110W	11534	3857	2347
2010-05-19 19:33:09	ACS/WFC	F475W	4747	1272	7076
2010-05-23 14:38:16	ACS/SBC	F140LP	1519	259	8296

Note. For the WFC3/IR observations, two F110W exposures were placed between two F160W exposures in each of the two orbits (see Section 2.1). The start times for these observations are for the first (of four) exposures in each filter, while the exposure times are for the summed F160W and F110W exposures. The last two rows refer to the observations reported by K+11. The wavelength λ_{piv} is the pivot wavelength as provided by HST, and the effective widths (defined as in C. Rodrigo et al. 2012) are taken from http://svo2.cab.inta-csic.es/svo/theory/fps/index.php?mode=browse.

filters (two orbits for each of the filters). In addition, we observed the target in a very broad F300X near-UV filter (two orbits) and in the F110W and F160W NIR filters. Since the F110W filter can suffer from unpredictable background variations from the He I airglow in the upper atmosphere,[5] we used a "sandwich observing strategy" for mitigation, placing the F110W exposures in the middle and the F160W exposures at the beginning and end of each of the two orbits. Images of the target vicinity in the five filters are shown in Figure 1. We used the drizzled images processed by the standard pipelines (calibration software caldp_20240509, CALWF3 version 3.7.1 for the WFC3 data, and AstroDrizzle version 3.7.0.). The pixel drizzle fractions are 1 for F110W, F160W, and F140LP and 0.8 for F300X and F475W; for details on the drizzling parameters, see the DrizzlePAC software documentation (A. S. Fruchter et al. 2010; S. Gonzaga et al. 2012).

[5] See WFC3 Instrument Science Report 2014-03: https://www.stsci.edu/files/live/sites/www/files/home/hst/instrumentation/wfc3/documentation/instrument-science-reports-isrs/_documents/2014/WFC3-2014-03.pdf.

2.2. XMM-Newton Observations

The XMM-Newton observations (ObsID 0935190301) were carried out on 2024 May 14 for 34.9 ks. Thin filters were used for all EPIC detectors. The EPIC-pn detector was in Large Window mode (frame time 47.7 ms); MOS1 and MOS2 were also in Large Window mode (frame time 0.9 s). We used XMM SAS version 21.0 for data analysis.

3. Data Analysis

3.1. UVOIR Spectrum of the Point-source Counterpart

3.1.1. Photometry

Photometry of J2143 in five HST filters is presented in Table 2, which provides the radii r_{extr} of the source apertures chosen and the corresponding fractions ϕ of point-source

Table 2
Photometry of the HST Observations of J2143

Filter	$t_{\rm exp}$ (s)	$r_{\rm extr}$ (arcsec)	ϕ (%)	$N_{\rm tot}$ (counts)	$N_{\rm bgd}$ (counts)	N_s (counts)	C_s (counts s^{-1})	$\mathcal{P}_\nu$ (nJy s count^{-1})	$\langle f_\nu \rangle$ (nJy)
F140LP	5098	0.175	60	229.5	19.9 ± 5.3	210 ± 15	0.0685 ± 0.0050	1651	113.1 ± 8.3
F140LP (K11)	8296	0.175	60	368.3	29.9 ± 5.6	338 ± 19	0.0680 ± 0.0064	1593	108.5 ± 6.2
F140LP (our+K11)[a]	13,394	0.175	60	585.0	48.5 ± 7.6	537 ± 24	0.0668 ± 0.0030	1651	110.2 ± 5.0
F300X	4926	0.15	76	611.8	97 ± 69	515 ± 72	0.138 ± 0.019	350	48.4 ± 6.8
F475W	4184	0.2	84	11,845	10,166 ± 210	1678 ± 214	0.478 ± 0.061	139	66.4 ± 8.5
F475W (K11)	7076	0.2	84	20,744	17,478 ± 184	3665 ± 192	0.617 ± 0.032	138	75.7 ± 4.5
F475W (our+K11)	11,260	0.2	84	32,445	27,524 ± 279	4922 ± 287	0.520 ± 0.030	139	72.3 ± 4.2
F110W	2347	0.47	86	107,758	104,975 ± 594	2783 ± 596	1.38 ± 0.30	68	93 ± 20
F160W	2497	0.47	85	61,529	59,082 ± 482	2446 ± 485	1.15 ± 0.23	153	177 ± 35

Notes. The rows marked "K11" provide the results of our photometry of the K+11 data, and the "our+K11" rows combine results from our and K+11 observations. The ϕ column provides the fractions of source counts in the apertures with radii $r_{\rm extr}$, $N_{\rm tot}$ is the total number of counts (electrons) in the source aperture, $N_{\rm bgd}$ and N_s are the background and net source count numbers in the chosen aperture, C_s is the aperture-corrected source count rate, $\mathcal{P}_\nu$ is the count-rate-to-flux conversion factor, and $\langle f_\nu \rangle$ is the characteristic flux density in the filter passband.
[a] Numbers of counts in the K+11 observation are divided over 1.036 to compensate for a higher SBC sensitivity in that observation.

counts in these apertures, taken from the respective online instrument handbook tables of encircled energy fractions. In each of the source apertures, we measured the total (source + background) count rate $C_{\rm tot}$ (in units of electrons s^{-1}) and converted it to the number of counts (electrons) $N_{\rm tot} = C_{\rm tot} t_{\rm exp}$. To measure the background and estimate the source count uncertainty, we used the "empty aperture" approach (e.g., R. E. Skelton et al. 2014). The background counts were measured in multiple apertures (from 40 to 115, depending on the filter) of the same size as the source aperture, uniformly distributed in source-free background regions. We calculated the mean $\overline{N}_{\rm bgd}$ and the variance $\sigma^2_{N_{\rm bgd}}$ of the measured numbers of counts in the background apertures and obtained the net source count number N_s and its uncertainty σ_{N_s}:

$$N_s = N_{\rm tot} - \overline{N}_{\rm bgd}, \qquad \sigma_{N_s} = \left(\sigma^2_{N_{\rm bgd}} + N_s\right)^{1/2}, \tag{1}$$

where $N_{\rm tot}$ is the total number of counts in the source aperture.

To convert the aperture-corrected pulsar's count number measured in a given filter, $N_s/(t_{\rm exp}\phi) = C_s$, to the mean flux density in that filter,

$$\langle f_\nu \rangle \equiv \frac{\int f_\nu(\nu)\mathcal{T}(\nu)\nu^{-1}\,d\nu}{\int \mathcal{T}(\nu)\nu^{-1}\,d\nu} = C_s \mathcal{P}_\nu\,, \tag{2}$$

we used the inverse sensitivity

$$\mathcal{P}_\nu = h\left[A_{\rm tel}\int \mathcal{T}(\nu)\nu^{-1}d\nu\right]^{-1}, \tag{3}$$

where h is the Planck constant, $A_{\rm tel}$ is the collecting area of the telescope, and $\mathcal{T}(\nu)$ is the dimensionless bandpass throughput function.[6] For an observation with a given filter, the conversion factor $\mathcal{P}_\nu$ is provided as the keyword `photfnu` in the data file header. Note that the mean flux density defined by Equation (2) is fully determined by the measured count rate and filter properties, and it is not tied to a specific wavelength within the passband.

To look for flux changes in the 14 yr since the K+11 observations, we applied the above-described approach to (re) measure the F140LP and F475W flux densities in those data and put the results in Table 2. Since we found no statistically significant changes in these filters, we combined the old and new observations to reduce the uncertainty.

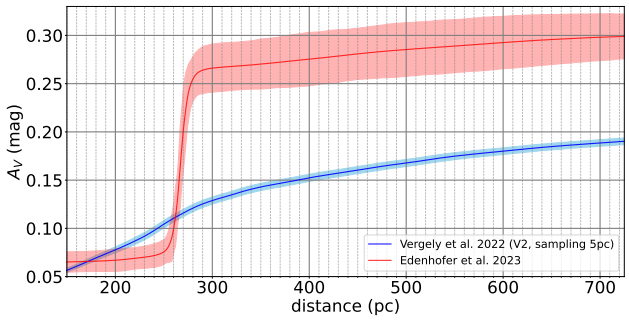

Figure 2. Dependence of the extinction coefficient A_V on distance in the direction to J2143. The blue line corresponds to data from J. L. Vergely et al. (2022), obtained via the G-Tomo tool (R. Lallement et al. 2022) that is available at ESA Datalabs. The red line shows the model by G. Edenhofer et al. (2024). Shaded regions mark the 3σ uncertainty ranges.

3.1.2. Extinction and Distance toward J2143

The shape of the observed UVOIR spectrum is affected by wavelength-dependent extinction caused by interstellar dust. With only five spectral bands and a strong correlation of the extinction coefficient with the spectral model parameters, we cannot measure the extinction from the UVOIR spectral fitting alone, but we may attempt to constrain it using other methods.

Extinction in a given direction depends on distance. This dependence can be found from 3D extinction maps (G. M. Green et al. 2019; R. H. Leike et al. 2020; R. Lallement et al. 2022; J. L. Vergely et al. 2022; G. Edenhofer et al. 2024). Different maps, however, may yield different results in some directions because of different angular and distance resolution and different methods used to construct the maps. For the direction toward J2143 (Galactic coordinates $l = 62.^\circ66$, $b = -33.^\circ14$), this is demonstrated in Figure 2, which shows the distance dependencies of the cumulative extinction coefficient A_V in the V band. The $A_V(d)$ curves with 3σ uncertainties, extracted from the maps by J. L. Vergely et al. (2022) and G. Edenhofer et al. (2024), are shown in blue and red, respectively. The main difference between them is the presence of a dust structure, centered at $d \sim 260$–270 pc, in

[6] See https://www.stsci.edu/files/live/sites/www/files/home/hst/documentation/_documents/SynphotManual.pdf, Chapter 7.

G. Edenhofer et al. (2024), which leads to a higher cumulative extinction at larger distances. A hint of a substantially larger diffuse structure at similar distances is barely seen in the extinction dependence obtained from the J. L. Vergely et al. (2022) map, which has a lower resolution. Interestingly, the $A_V(d)$ curves obtained from the maps of G. M. Green et al. (2019) and R. H. Leike et al. (2020) are very close to the J. L. Vergely et al. (2022) curve, but the high-resolution dust emission data obtained with the Planck observatory shows a complex structure in that direction and $A_V \approx 0.27$ at infinity (R. Lallement 2025, private communication). Given the higher resolution of the G. Edenhofer et al. (2024) map and its consistency with the Planck map, we consider this $A_V(d)$ dependence more reliable and use it in the following analysis.

The distance to J2143 has not been directly measured. S. Zane et al. (2005) suggest $d \sim 280$ pc from the assumption that its X-ray luminosity is close to a "typical" XTINS luminosity, $L_{0.1-2.4\,\mathrm{keV}} \sim 5 \times 10^{31}\,\mathrm{erg\,s^{-1}}$. Given the large scatter of XTINS luminosities, this distance estimate can be off by a factor of ~2–3. However, extinction (and hence distance) can be constrained from the hydrogen column density N_H estimated from X-ray spectral fits using a linear correlation between N_H and A_V (D. R. Foight et al. 2016 and references therein). A problem with this approach is the strong dependence of N_H on the model used for fitting the X-ray spectra of J2143—most of the explored models give[7] $N_{\mathrm{H},20} \equiv N_\mathrm{H}/(10^{20}\,\mathrm{cm^{-2}}) \approx 2$–5. Using the correlation $N_{\mathrm{H},20} = (28.7 \pm 1.2)A_V$ (D. R. Foight et al. 2016), this range of N_H corresponds to $A_V \approx 0.07$–0.18. This broad extinction range corresponds to a relatively narrow distance range, $d \approx 240$–270 pc, as follows from the G. Edenhofer et al. (2024) curve $A_V(d)$ in Figure 2. Thus, even with accounting for the large scatter in the N_H–A_V correlation, particularly strong at small distances, it looks plausible that J2143 is an NS embedded in the nearby dust cloud. In further analysis, we will investigate the dependencies of the J2143 parameters on extinction and distance around the fiducial values $A_V = 0.12$ and $d = 260$ pc.

3.1.3. UVOIR Spectral Fits

To fit a spectral model f_ν^mod to the measured count rates in the five filters, we calculate the model count rates as a function of the model parameters,

$$C_i^\mathrm{mod} = (A_\mathrm{tel}/h)\int f_\nu^\mathrm{mod}\,\mathcal{T}_i(\nu)\nu^{-1}\,d\nu\,, \tag{4}$$

with the aid of filter throughputs $\mathcal{T}_i(\nu)$ produced by `synphot` and find the parameter values that minimize the χ^2 statistic

$$\chi^2 = \sum_{i=1}^{5}\frac{(C_i^\mathrm{mod} - C_i)^2}{\sigma_{C_i}^2}\,, \tag{5}$$

where $C_i = N_{s,i}/(\phi_i t_{\mathrm{exp},i}) = C_{s,i}$ is the measured source count rate in the ith passband.

As we immediately see from the data points in Figure 3, the spectrum is qualitatively different from a simple PL or a thermal spectrum. However, it can be described as a sum of a PL component and an R-J tail of a thermal component at lower and higher frequencies, respectively, similar to the UVOIR spectra of RPPs (see, e.g., V. Abramkin et al. 2025 and references therein). Therefore, we will fit it with the absorbed PL + BB model,

$$f_\nu^\mathrm{mod} = \left[f_0\left(\frac{\nu}{\nu_0}\right)^\alpha + \frac{R_\mathrm{uv}^2}{d^2}\pi B_\nu(T_\mathrm{uv})\right]10^{-0.4A_\nu}\,, \tag{6}$$

where ν_0, f_0, and α are the reference frequency, normalization, and slope of the PL component; d is the distance; $B_\nu(T_\mathrm{uv})$ is the Planck function; and R_uv is the radius of an equivalent sphere in the UV range, i.e., a sphere with a uniform surface temperature T_uv that emits pure BB radiation. The surface temperature of a real NS can be nonuniform because of anisotropy of thermal conduction in a strong magnetic field, and its thermal emission can differ from the pure BB emission (e.g., J. F. Pérez-Azorín et al. 2005). Therefore, Equation (6) should be considered as a phenomenological model in which T_uv is an estimate of an average surface temperature measurable in the UV range, while R_uv can be substantially smaller than the true NS radius (see Section 4.2 for further discussion).

We choose $\nu_0 = 1 \times 10^{15}$ Hz (corresponding to $\lambda_0 = 3000$ Å). We take the frequency dependence of the extinction A_ν from K. D. Gordon et al. (2023) and normalize it by the extinction value A_V in the V band, adopting $A_V = 0.12$ as a fiducial value (see Section 3.1.2).

The thermal term in Equation (6) can be written as

$$\left(\frac{R_\mathrm{uv}}{d}\right)^2\pi B_\nu(T_\mathrm{uv}) = 7.2\frac{(R_{10}/d_{260})^2\nu_{15}^3}{\exp(h\nu/kT_\mathrm{uv}) - 1}\,\mathrm{nJy}\,, \tag{7}$$

where $R_{10} = R_\mathrm{uv}/10$ km, $d_{260} = d/260$ pc, and $\nu_{15} = \nu/10^{15}$ Hz. The model (Equation (6)) has five parameters. However, in the R-J regime, $h\nu \ll kT_\mathrm{uv}$, the model spectrum and the χ^2 value depend on the so-called R-J parameter, $kT_\mathrm{uv}(R_\mathrm{uv}/d)^2$ (G. G. Pavlov et al. 1997), rather than on T_uv and R_uv/d separately. Since the R-J parameter strongly correlates with the extinction, we fit the model to the five data points at fixed extinction values, varying three model parameters.

Figure 3 shows an example of the PL+BB fit at $A_V = 0.12$, $R_{10}/d_{260} = 1$. The best-fit PL component, $f_\nu = f_0\,\nu_{15}^\alpha$, decreases with frequency—e.g., $\alpha = -0.80 \pm 0.15$ at $A_V = 0.12$. The PL

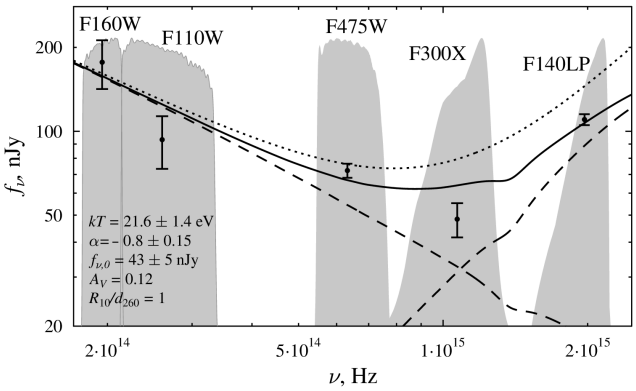

Figure 3. UVOIR spectrum of J2143. The data points with vertical error bars show the measured mean flux densities $\langle f_\nu\rangle$ with the statistical 1σ errors; they are plotted at pivot wavelengths. The shaded areas show the filter throughputs (arbitrarily scaled). The solid curve shows the best fit for the PL+BB model (see Equation (6)) for $A_V = 0.12$ at the fixed $R_{10}/d_{260} = 1$. The dashed curves show the PL and BB components. The dotted curve shows the dereddened best-fit spectrum.

[7] There is an outlier, $N_{\mathrm{H},20} = 13.2 \pm 0.9$, in A. Mancini Pires et al. (2023), which was likely caused by poorly known calibration of the eROSITA detectors at low X-ray energies.

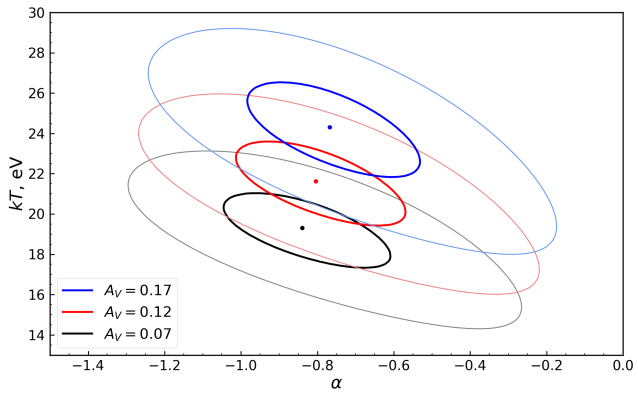

Figure 4. Confidence contours for the UVOIR spectral fit with the PL+BB model (see Figure 3) at the 68.3% and 99.7% confidence levels (for two parameters of interest) in the α–kT plane for $R_{10}/d_{260} = 1$ at the extinction values shown in the legend.

slope slightly steepens with increasing extinction, as seen in Figure 4, but for a reasonable extinction interval, $0.05 \lesssim A_V \lesssim 0.2$, the change of the best-fit α is smaller than its 1σ uncertainty.

The thermal component dominates in the UV range, at $\lambda \lesssim 3000$ Å. Taking into account that the brightness temperature in the R-J regime is proportional to $(d/R)^2$, the fit shown in Figure 3 corresponds to $kT_{\rm uv} \sim \mathbf{22}(d_{260}/R_{10})^2$ eV; i.e., this brightness temperature is rather uncertain because the equivalent sphere radius is unknown. An additional (smaller) temperature uncertainty is due to extinction uncertainty. According to Figure 4, the temperature slightly increases with increasing A_V. Additional constraints on the surface temperature and NS thermal emission can be obtained from analysis of the X-ray emission and from joint fits of the UVOIR and X-ray spectra, provided below.

3.2. Possible Extended Emission in the NIR Bands

As can be seen in Figure 1, there seems to be a hint of flux enhancement around the pulsar in the NIR images. Using a polygon aperture (area of $\approx$13 arcsec^2; see the Appendix for details), we measure net flux densities $f^{\rm ext}_{\rm F160W} = 1.69 \pm 0.25$ μJy and $f^{\rm ext}_{\rm F110W} = 0.88 \pm 0.17$ μJy in the F160W and F110W filters, respectively, where the errors only reflect statistical uncertainties. Neglecting the possible contribution of unrecognized faint sources and assuming a PL spectral shape ($f^{\rm ext}_\nu \propto \nu^{\alpha_{\rm ext}}$), the supposed extended emission has a spectral index of $\alpha_{\rm ext} = -2.27 \pm 0.83$.

3.3. XMM-Newton Data Analysis

3.3.1. Timing Analysis

In order to check for possible variability of the X-ray pulsations of J2143, such as reported by A. Mancini Pires et al. (2023), we carried out a timing analysis of the EPIC data. We removed data obtained during the largest background flare and used the remaining counts from the energy range 0.15–2 keV (single and double patterns for pn and patterns 0–12 for MOS), extracted from circles with 47″ and 40″ radii for the pn and MOS detectors, respectively.

We applied the binning-free Fourier analysis to barycenter-corrected times of arrival as described in the Appendices of J. Hare et al. (2021) and B. Posselt et al. (2024). This analysis

Table 3
Fourier Amplitudes and Phases and Z^2_k Statistics for the First Four Harmonics at $\nu = 0.1060619$

k	1	2	3	4
		pn + MOS1&2		
s_k	0.0269(49)	0.0067(49)	0.0188(49)	0.0080(49)
ψ_k	0.076(29)	0.37(12)	0.230(42)	0.58(10)
Z^2_k	29.5	31.4	45.7	48.2
		pn only		
s_k	0.0258(55)	0.0099(55)	0.0135(56)	0.0071(56)
ψ_k	0.060(34)	0.46(9)	0.219(65)	0.56(12)
Z^2_k	21.6	24.8	30.7	32.3

Note. The numbers in parentheses are 1σ uncertainties of the last digits of the measured quantities. The amplitude and phase uncertainties are estimated as $\sigma_{s_k} = (2/N)^{1/2}$ and $\sigma_{\psi_k} = (2\pi s_k)^{-1}(2/N)^{-1/2}$, where N is the number of counts (B. Posselt et al. 2024).

starts from calculating the empirical Fourier coefficients,

$$a_k = \frac{2}{N}\sum_{i=1}^{N} \cos 2\pi k\phi_i = s_k \cos 2\pi\psi_k, \quad (8)$$

$$b_k = \frac{2}{N}\sum_{i=1}^{N} \sin 2\pi k\phi_i = s_k \sin 2\pi\psi_k, \quad (9)$$

where s_k and ψ_k are the amplitude and phase of the kth harmonic, $\phi_i = \nu_{\rm trial}(t_i - t_{\rm ref})$, t_i is the time of arrival of the ith count, $t_{\rm ref}$ is the reference epoch, and $\nu_{\rm trial}$ is the trial frequency. The empirical signal frequency ν is the trial frequency value at which the Fourier power $Z^2_K = (N/2)\sum_{k=1}^{K} s^2_k$, summed over statistically significant harmonics, is maximal.

In our case, harmonics $k \geqslant 4$ are not statistically significant (i.e., $K = 3$), and the empirical signal frequency is $\nu = 0.1060619(13)$ Hz, fully consistent with the ephemeris derived by S. Bogdanov & W. C. G. Ho (2024) from observations of 2004–2023. The frequency uncertainty, $\sigma_\nu = 1.3 \times 10^{-6}$ Hz, is estimated from Equation (A24) of B. Posselt et al. (2024).

Table 3 shows the values of the empirical Fourier amplitudes and phases, as well as the sums of Fourier powers, for the first four harmonics at the measured frequency. In the upper half of the table, the Fourier parameters were calculated from the pn + MOS1&2 data ($N = 81{,}654$ counts, $T_{\rm span} = 33.2$ ks), which we used for measuring the frequency. Since the time resolution of the MOS data is too crude to analyze harmonics $k \geqslant 3$, in the lower half of the table, we show the same Fourier parameters for the pn data only ($N = 64{,}848$ counts, $T_{\rm span} = 31.3$ ks). Notice that $s_3 > s_2$ in both cases; i.e., the third harmonic is more powerful than the second one.

We used the pn-only Fourier amplitudes and phases to plot the folded light curve (pulse profile) of J2143 (solid blue curve in Figure 5). The profile is very similar to that found by S. Bogdanov & W. C. G. Ho (2024) from multiple observations, including possible smaller peaks at $\Delta\phi \approx \pm 0.3$ with respect to the main peak. An example of a traditional binned light curve, plotted in the same figure, shows good agreement with the binning-free profile.

The Fourier amplitudes directly provide the rms pulsed fraction, $p_{\rm rms} = [\sum_k (s^2_k/2)]^{1/2}$ (J. Hare et al. 2021). Including

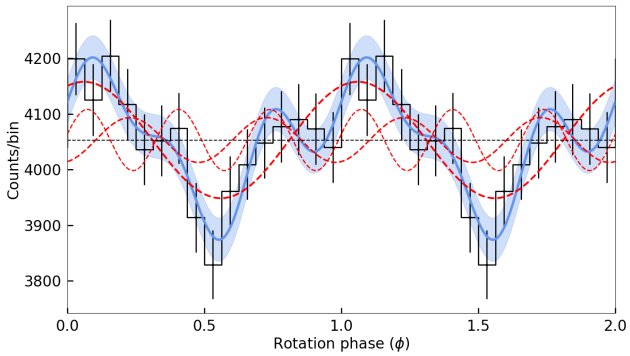

Figure 5. Pulsations of J2143 with frequency $\nu = 0.1060619$ Hz in the 0.15–2 keV energy range, obtained from the EPIC-pn data. The red dashed lines display the $k \leqslant 3$ Fourier harmonics. The solid blue line shows their sum; its 68% uncertainty is indicated by the shaded area. The horizontal dotted line at 4053 counts bin^{-1} shows the constant component of the phase-folded light curve. The zero phase corresponds to the epoch MJD 60443.6296296 (TDB). The histogram demonstrates the more traditional binned profile, with 16 bins.

the $k \leqslant 3$ terms in the sum, we obtain $p_{\rm rms} = 2.2(4)\%$. Using the unbinned and binned light curves, we also calculated the area and amplitude pulsed fractions,[8] $p_{\rm area} = 4.4(9)\%$ and $p_{\rm amp} = 4.1(8)\%$, where the uncertainties were estimated from Monte Carlo simulations. While the 3σ uncertainty range allows the lower $p_{\rm amp} = 2.5\%$ reported by A. Mancini Pires et al. (2023) from eROSITA observations, our results are closer to the previously reported $p_{\rm amp} \approx 4\%$ that was also based on XMM-Newton observations (S. Zane et al. 2005; D. L. Kaplan & M. H. van Kerkwijk 2009b). Thus, we do not see significant changes in the X-ray pulsations of J2143 in the XMM-Newton observations.

3.3.2. Spectral Analysis

In order to understand the multiwavelength emission from J2143, we analyzed the spectra obtained by the EPIC detectors in our contemporaneous XMM-Newton observation, both separately and together with the UVOIR spectra. After removing two background flares, the effective exposure times are 27.3 and 23.5 ks for the EPIC-pn and MOS1&2 detectors, respectively. Pattern analysis with the task `epatplot` showed only very minor pileup in the target for EPIC-pn. To minimize the effects of calibration uncertainties, we use only single events for EPIC-pn. After employing the task `eregionanalyse`, the EPIC-pn and MOS1&2 source spectra were extracted from circular regions with radii of 47″ and 40″ and patterns 0 and 0–12, respectively. We chose background regions on the same chips as the source regions. Within an energy range of 0.2–2 keV, we obtain net (source) count rates of 1.767 ± 0.008, 0.343 ± 0.004, and 0.313 ± 0.004 cps for EPIC-pn, MOS1, and MOS2, respectively.

We employ the XSPEC package (ver. 12.13.0) to fit the observed spectra. To describe the interstellar absorption, we use the `tbabs` model with abundances from J. Wilms et al. (2000). As no source counts are seen above 2 keV, we fit the spectrum in the 0.2–2 keV band. To compare with the previous works, we fit the spectra with one- or two-component BB models (`bbodyrad` in XSPEC) with up to two multiplicative `gabs` models included to describe possible absorption features.

The fit results, presented in Table 4, are close to those obtained by S. Zane et al. (2005), M. Cropper et al. (2007), D. L. Kaplan & M. H. van Kerkwijk (2009b), and A. D. Schwope et al. (2009) from previous observations. The single BB model without spectral features, 1BB0G, leaves large residuals around 0.7 keV. Including one `gabs` component (1BB1G model),

$$\texttt{gabs}(E) = \exp\left[-\frac{s}{\sqrt{2\pi}\,\sigma}\exp\left(-\frac{(E-E_c)^2}{2\sigma^2}\right)\right], \qquad (10)$$

we obtain a better fit, with about the same BB temperature $kT \approx 106$ eV and radius $R \approx 1.5 d_{260}$ km. The absorption line is centered at $E_c = 0.74$ keV; its rather uncertain Gaussian width, $\sigma \sim 4$–33 eV, is smaller than the energy resolution of the EPIC detectors. The third `gabs` parameter s, called "depth" in the XSPEC description, is proportional to the optical depth τ at the line center, $s \equiv (2\pi)^{1/2}\sigma\tau$, and it is close to the line's equivalent width at $\tau \lesssim 1$. The s–σ confidence contours show that $s \sim 15$–20 eV ($\tau \sim 0.1$–1) for a more realistic $\sigma \sim 8$–33 eV, but it may reach ~48 eV at very low $\sigma \sim 4$ eV.

Including a second `gabs` line (1BB2G model), suggested by M. Cropper et al. (2007), slightly improves the fit without a significant effect on the properties of the thermal component and the 0.74 keV line. The second line is centered at ~0.4 keV, and its σ and s parameters are even smaller than those of the 0.74 keV line.

Following A. D. Schwope et al. (2009), who suggested the presence of a second BB component with a lower temperature, we also added such a component for models with one and two `gabs` lines (2BB1G and 2BB2G models). However, fits with these models are very unstable, and the fitting parameters are very uncertain (so that we had to fix some of the fitting parameters to estimate the uncertainties of others). The best-fit radii of the second BB component are unrealistically large, particularly for the 2BB1G models, which means that we should not trust other fitting parameters (e.g., the elevated $N_{\rm H}$ values). Obviously, such models have too many parameters for the narrow energy range and the number of counts available.

We found that for each of the explored models, the observed (absorbed) energy flux is about the same, $F_{0.2\text{–}2\,\rm keV} \simeq 2.8 \times 10^{-12}$ erg cm^{-2} s^{-1}, within a 1.4% relative uncertainty. This value is consistent with the previous X-ray flux measurements, as well as the spectral parameters. Thus, the spectral and flux properties of J2143 at our observing epoch are consistent with those of the previous 20 yr of XMM-Newton observations.

3.4. Joint Spectral Fit of the HST and XMM-Newton Data

Assuming that the same two BB components can contribute to the flux spectrum at both X-ray and UVOIR frequencies, we added a UVOIR PL component to the 2BB1G and 2BB2G models and fitted the combined models in the 0.5 eV–2 keV range. The fitting parameters for these models are shown in the last two columns of Table 4, while the UVOIR through X-ray absorbed energy flux spectrum f_ν and the spectral energy distribution (SED) $\nu f_\nu^{\rm unabs}$ are shown in Figures 6 and 7, respectively. Thanks to adding the UVOIR data, the parameters for the $\rm BB_{cold}$ component are much better constrained than for the X-ray fits alone. Contrary to the UVOIR-only fit, which only

[8] The area pulsed fraction, $p_{\rm area}$, is defined as the ratio of areas under the varying part of the light curve to the total area, while the amplitude pulsed fraction, $p_{\rm amp}$ (sometimes called the "peak-to-peak" or "max-to-min" pulsed fraction), is the difference between the maximum and minimum values of the pulse profile to their sum; see J. Hare et al. (2021) for details.

Table 4
Spectral Fits of the X-Ray and X-Ray + UVOIR Data

	1BB0G	1BB1G	1BB2G	2BB1G	2BB2G	2BB1G+PL	2BB2G+PL
$N_{\rm H}$ (10^{20} cm^{-2})	2.0 ± 0.2	2.1 ± 0.2	1.9 ± 0.2	$9.0^{+2.5}_{-1.5}$	$8.5^{+2.1}_{-1.8}$	2.6 ± 0.5	$3.5^{+0.5}_{-0.8}$
$kT_{\rm hot}$ (eV)	105.9 ± 0.5	106.5 ± 0.5	106.1 ± 0.5	100 ± 2	101 ± 2	105.9 ± 1.3	105.2 ± 0.5
$R_{\rm hot}/d_{260}$ (km)	1.52 ± 0.03	1.52 ± 0.03	1.53 ± 0.03	2.2 ± 0.2	2.1 ± 0.3	$1.56^{+0.11}_{-0.12}$	$1.62^{+0.03}_{-0.04}$
$L_{\rm hot}/d^2_{260}$ (10^{31} erg s^{-1})	3.7	3.8	3.8	6.3	6.0	4.0	4.1
$kT_{\rm cold}$ (eV)	⋯	⋯	⋯	29 ± 2	33^{+4}_{-3}	38^{+4}_{-6}	48^{+3}_{-8}
$R_{\rm cold}/d_{260}$ (km)	⋯	⋯	⋯	160^{+150}_{-80}	70^{+100}_{-40}	$6.4^{+0.6}_{-0.5}$	5.9 ± 0.4
$L_{\rm cold}/d^2_{260}$ (10^{31} erg s^{-1})	⋯	⋯	⋯	230	80	1.1	2.3
E_{c1} (eV)	⋯	740 ± 8	739 ± 8	753 ± 7	752 ± 7	741 ± 7	741 ± 7
σ_1 (eV)	⋯	19^{+14}_{-15}	22^{+13}_{-17}	50^{+16}_{-12}	43 ± 18	22^{+12}_{-18}	23^{+13}_{-19}
s_1 (eV)	⋯	18^{+30}_{-3}	19^{+15}_{-3}	35^{+11}_{-7}	30 ± 10	19^{+23}_{-3}	18^{+55}_{-2}
E_{c2} (eV)	⋯	⋯	400 ± 11	⋯	392 ± 17	⋯	403 ± 10
σ_2 (eV)	⋯	⋯	5^{+18}_{-4}	⋯	<25	⋯	10^{+20}_{-9}
s_2 (eV)	⋯	⋯	$9^{+?}_{-3}$	⋯	$16^{+?}_{-12}$	⋯	$10^{+?}_{-4}$
$A_V = 0.035N_{\rm H,20}$	⋯	⋯	⋯	⋯	⋯	0.09 ± 0.05	0.12 ± 0.03
α	⋯	⋯	⋯	⋯	⋯	-0.78 ± 0.16	-0.74 ± 0.15
f_{ν_0} (nJy)	⋯	⋯	⋯	⋯	⋯	44 ± 7	46 ± 6
$L_1 - 10\,{\rm eV}/d^2_{260}$ (10^{28} erg s^{-1})	⋯	⋯	⋯	⋯	⋯	0.8	0.8
$C_{\rm mos1}$	1.113 ± 0.015	1.109 ± 0.015	1.113 ± 0.015	1.107 ± 0.015	1.108 ± 0.015	1.109 ± 0.015	1.110 ± 0.014
$C_{\rm mos2}$	1.152 ± 0.016	1.153 ± 0.016	1.156 ± 0.016	1.151 ± 0.016	1.152 ± 0.016	1.153 ± 0.016	1.154 ± 0.016
χ^2_ν [dof]	1.82 [103]	1.27 [100]	1.15 [97]	1.15 [98]	1.15 [95]	1.32 [101]	1.22 [98]

Note. The abbreviation mBBnG denotes the model with m additive BB components and n multiplicative `gabs` components describing absorption lines for the Gaussian absorption coefficient; in the 2BBnG+PL models, a UVOIR PL component is added. Each BB component is characterized by the temperature kT, equivalent sphere radius R, and bolometric luminosity $L = 4\pi\sigma R^2 T^4$ for an assumed distance $d = 260$ pc; the radii are calculated from the `bbodyrad` norm $K_{\rm BB} = R^2_{\rm km}/d^2_{10\,\rm kpc}$. The ith `gabs` component is characterized by the central energy E_{ci}, Gaussian width σ_i, and "depth" s_i (see Equation (10)). For the PL component, $f_\nu = f_0(\nu/\nu_0)^\alpha 10^{-0.4A_V}$, we assume the optical extinction to be tied to the hydrogen column density, $A_V = 0.035N_{\rm H,20}$ (D. R. Foight et al. 2016); choose $\nu_0 = 10^{15}$ Hz ($h\nu_0 = 4.14$ eV); and calculate the UVOIR luminosity $L_{1-10\,\rm eV}$. The coefficients $C_{\rm mos1}$ and $C_{\rm mos2}$ are additional normalization factors for the MOS count rates relative to the pn normalization. The last row provides the minimum reduced χ^2 values and the numbers ν of degrees of freedom (dof). Uncertainties indicate the 68% confidence levels.

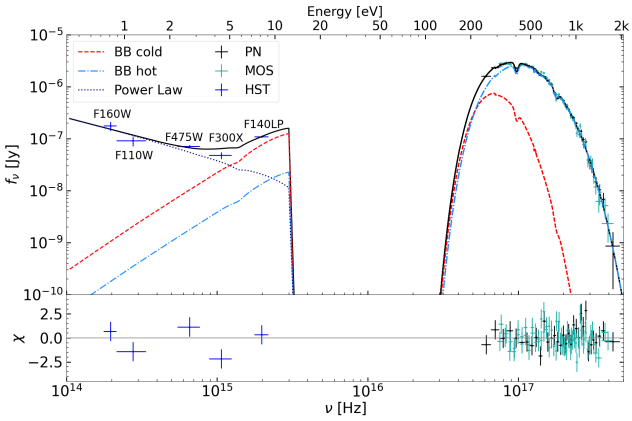

Figure 6. Unfolded XMM-Newton EPIC and HST spectrum of J2143 compared with the best-fit 2BB2G+PL model that includes the ISM absorption/extinction, $\rm BB_{hot}$ and $\rm BB_{cold}$ components, two absorption features in soft X-rays, and the UVOIR PL component. The fit parameters are listed in Table 4. The lower panel shows the fit residuals defined as χ = (data − model)/error.

provides a brightness temperature $\propto (d/R)^2$, the best-fit temperatures in the joint fits are derived from both the R-J and Wien parts of the BB spectra. Therefore, we can measure the R/d ratio and the temperatures separately, despite a correlation between these parameters.

The parameters of the $\rm BB_{hot}$ component and the absorption features in the joint X-ray + UVOIR fits are close to those obtained from the X-ray fits with the 1BBnG models: $kT_{\rm hot} \approx 105$–106 eV, $R_{\rm hot}/d_{260} \approx 1.5$–$1.6$ km, $E_{c1} \approx 0.73$–0.75 keV, $E_{c2} \approx 0.39$–0.41 keV, etc. The "cold radius" values, $R_{\rm cold}/d_{260} \approx 5.5$–$7$ km, are much lower, while the "cold temperature" values, $kT_{\rm cold} \approx 30$–50 eV, are substantially higher than for the 2BBnG models. We see from Figures 6 and 7 that the FUV emission is dominated by the $\rm BB_{cold}$ component, but both the $\rm BB_{hot}$ and the PL components also contribute at the $\sim$10% level each. The slope $-0.9 \lesssim \alpha \lesssim -0.6$ of the UVOIR PL component, which dominates in the IR and optical ranges, is very close to that obtained from the UVOIR-only fit with the PL+BB model. Thus, we have shown that the phenomenological 2BBnG +PL models for the UVOIR + X-ray spectrum provide satisfactory fits with reasonable parameter values, better constrained than is possible for separate UVOIR and X-ray datasets. The 2BB2G+PL model fits somewhat better than the 2BB1G+PL model, which can be considered as a justification for the additional spectral feature at $\approx$0.4 keV.

3.5. Proper Motion of J2143

Comparison of our and K+11's ACS/WFC F475W images, carried out in the same observational setup on MJD 60448.9 and MJD 55335.9, allows one to measure the proper motion of J2143 with minimal distortion effects and good astrometric boresight correction possibility. For the latter, we use the Gaia Data Release 3 (DR3; Gaia Collaboration et al. 2023, 2016) to identify 18 suitable reference sources in the field of view. We applied the catalog proper motions to calculate the positions of the selected Gaia DR3 stars at the two epochs. Using the

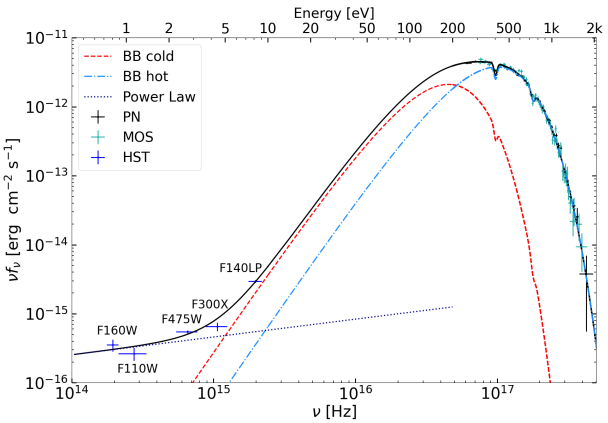

Figure 7. SED for the UVOIR through X-ray emission for the same model as in Figure 6.

Graphical Astronomy and Image Analysis Tool (M. J. Currie et al. 2014), we obtain a fit of the image astrometry with the proper-motion-corrected Gaia DR3 catalog positions.

The rms of the respective fit residuals is used as the systematic astrometric error (with respect to the common Gaia DR3 reference frame). Centroid errors for the pulsar positions are obtained using FWHM values from 2D Gaussian fits and the peak signal-to-noise ratio of the detections according to Equation (1) in M. J. Reid et al. (1988).

The two HST positions in Table 5 are separated by 80.8 ± 7.7 mas. The proper-motion components along R.A. and decl. are[9]

$$\mu_\alpha = 4.3 \pm 0.5 \ \text{mas yr}^{-1}, \quad \mu_\delta = -3.8 \pm 0.5 \ \text{mas yr}^{-1}. \tag{11}$$

This is equivalent to $\mu = 5.8 \pm 0.5$ mas yr^{-1} with a position angle P.A. $= 131.^\circ3 \pm 5.^\circ5$ (east of north; see Figure 1).

In Galactic coordinates, the proper-motion vector is $\mu_l = -0.2 \pm 0.5$ mas yr^{-1}, $\mu_b = -5.8 \pm 0.5$ mas yr^{-1}; i.e., J2143 (Galactic latitude of $b = -33.^\circ1$) is moving away from the Galactic plane. At a fiducial distance of 260 pc, this proper motion corresponds to a transverse velocity of 7.1 ± 0.7 km s^{-1}.

4. Discussion

Our HST observations have shown that the observed broadband UVOIR spectrum of J2143 can be described by a sum of a thermal component, dominating at UV wavelengths, and a PL component, dominating in the NIR–optical (see Figure 3). Such a two-component UVOIR spectrum strongly resembles those of middle-aged RPPs (see V. Abramkin et al. 2025 and references therein), but it has not been clearly seen in XTINSs so far. Below, we discuss the thermal and PL components, taking the contemporaneous X-ray data into account.

4.1. Nonthermal UVOIR Emission

The HST observations of J2143 in five spectral bands allowed us to discover a component with a PL-like spectrum, $f_\nu = f_0 (\nu/\nu_0)^\alpha$, $f_0 = 40$–50 nJy at $\nu_0 = 10^{15}$ Hz, $-\alpha = 0.6$–1.0. It resembles the nonthermal components detected in UVOIR emission of several middle-aged RPPs (see Table 4 and Figure 8 in V. Abramkin et al. 2025), with spectral slopes $-0.5 \lesssim \alpha \lesssim -0.1$ and typical luminosities $L^{\rm nonth}_{1-10\,\rm eV} \equiv 4\pi d^2 F^{\rm nonth}_{1-10\,\rm eV} \sim (2\text{–}7) \times 10^{28}$ erg s^{-1}, where $F^{\rm nonth}_{1-10\,\rm eV}$ is the unabsorbed nonthermal energy flux in the 1–10 eV band. Those components are usually interpreted as emission from relativistic particles in pulsar magnetospheres, powered by the pulsar's rotational energy loss rate $\dot{E}$. The fraction of $\dot{E}$ converted into the UVOIR emission is characterized by the efficiency $\eta_{1-10\,\rm eV} \equiv L^{\rm nonth}_{1-10\,\rm eV}/\dot{E} \sim (0.5\text{–}5) \times 10^{-6}$.

In the case of J2143, the UVOIR PL flux, luminosity, and efficiency are

$$F^{\rm PL}_{1-10\,\rm eV} = (8 - 11) \times 10^{-16} \ \text{erg cm}^{-2} \ \text{s}^{-1}, \tag{12}$$

$$L^{\rm PL}_{1-10\,\rm eV} = (6 - 9) \times 10^{27} d^2_{260} \ \text{erg s}^{-1}, \tag{13}$$

$$\eta^{\rm PL}_{1-10\,\rm eV} = (3 - 5) \times 10^{-3} d^2_{260}; \tag{14}$$

i.e., the luminosity of J2143 is lower but the efficiency is much higher than those of middle-aged RPPs.

Unlike RPPs, J2143 does not exhibit nonthermal emission in X-rays and γ-rays. C. Dessert et al. (2020) derived a flux upper limit of 7.4×10^{-16} erg cm^{-2} s^{-1} in the energy range 2–4 keV, which is below the extrapolation of the UVOIR PL with the same slope. It is possible that the nonthermal f_ν spectrum steepens with increasing energy, as we observe in middle-aged RPPs, but an X-ray detection would be difficult even for very deep observations.

The differences between the alleged magnetospheric emission of J2143 and middle-aged RPPs could be associated with the longer period and lower spin-down power of the former, which may lead to a smaller number of particles accelerated to high energies and a larger number of particles (and emitted photons) of lower energies. However, the lower spin-down power alone cannot be the cause of J2143's missing nonthermal X-ray and radio emission. Radio efficiency actually increases with lower spin-down power (B. Posselt et al. 2023), and very old pulsars with comparably low spin-down power exhibit detectable nonthermal X-ray emission components (B. Posselt et al. 2012). On the other hand, the effect of the long period (e.g., on the Goldreich–Julian charge density) could be counterbalanced by the stronger magnetic field, which should facilitate particle acceleration. Although the actual emission mechanism in the UVOIR range remains unknown, it is possible that J2143 is a high-B, low-power cousin of ordinary middle-aged RPPs whose nonthermal X-ray emission is simply below our detection threshold. The lack of γ-ray emission from J2143 can be explained by the low spin-down power, while the apparent lack of observable radio emission (V. I. Kondratiev et al. 2009) could be due to unfavorable orientations of its rotation and magnetic axes or extreme faintness of the radio emission.

We note that in some respects, J2143's UVOIR PL component resembles that detected with JWST from the magnetar 4U 0142 +61, with the slope $\alpha = -0.96 \pm 0.02$ (J. Hare et al. 2024). If that emission is powered by the NS rotation energy loss, then the IR efficiency is as high as $\eta_{1.4-11\,\mu\rm m} \approx 0.6 (d/3.6\,\rm kpc)^2$, which corresponds to $\eta_1 - 10\,\rm eV \approx 0.7 (d/3.6\,\rm kpc)^2$ if the IR–optical spectrum is extrapolated to the UV range. Thus, in terms of efficiency, J2143 could be an intermediate object between the usual RPPs and magnetars. We caution, however, that the magnetar's UVOIR emission can be powered by a mechanism different from the rotation energy loss, in which case the above-defined efficiency becomes irrelevant.

[9] Note that some authors use the notations $\mu_\alpha \cos\delta$ and $\mu_l \cos b$ instead of μ_α and μ_l.

Table 5
Pulsar Astrometry for the ACS/WFC F475W Data

Epoch	Pixel Scale (mas pixel^{-1})	$\sigma_{\rm bsc}^{\rm radial}$ (mas)	$\sigma_{\rm cent}^{\rm radial}$ (mas)	$\alpha - \alpha_0$	$\delta - \delta_0$	$\sigma^{\rm radial}$ (mas)	$\sigma^{\rm 1D}$ (mas)
2010.4	50	6.9	0.4	3$^{\rm s}$39104	17.″4268	6.9	4.5
2024.4	50	9.4	0.9	3$^{\rm s}$39512	17.″3735	9.4	6.2

Note. The fit to the Gaia DR3 counterparts of 18 field stars resulted in the pulsar's R.A. α and decl. δ, counted from $\alpha_0 = 21^{\rm h}43^{\rm m}00^{\rm s}$ and $\delta_0 = 6^\circ\,54'\,00''$. The systematic radial uncertainty $\sigma_{\rm bsc}^{\rm radial}$ is the uncertainty of the boresight correction with the 18 stars, $\sigma_{\rm cent}^{\rm radial}$ indicates the centroiding radial uncertainty, $\sigma^{\rm radial}$ is the total radial uncertainty, and $\sigma^{\rm 1D}$ is the uncertainty in one coordinate component. All the uncertainties are at the 68% confidence level.

In principle, the PL UVOIR component in the J2143 emission might be due to an unusual PWN that is not seen outside of the UVOIR range. Support for this interpretation might be provided by a confirmation of the extended emission around the point source, possibly seen in the two NIR filters (see Section 3.2). Such an explanation could be verified observationally by a search for UVOIR pulsations,[10] but such a search is hardly feasible with the currently available instruments because of the faintness of J2143 in the UVOIR.

Yet another possibility might be that the UVOIR PL component $f_\nu \propto \nu^\alpha$ is emitted from a fallback disk with the temperature decreasing outward as $T \propto r^{-\beta}$, where $\beta = 2/(3 - \alpha)$ (e.g., $\beta = 0.526$ for $\alpha = -0.8$); see, for instance, Ü. Ertan et al. (2017) and J. Hare et al. (2024). This hypothesis can be tested with IR observations at longer wavelengths.

To establish the true nature of the discovered PL UVOIR emission, it would be, of course, very important to understand how common such emission is among XTINSs (and perhaps high-B RPPs with similar properties). Indirect evidence for such emission is provided by the results of K+11, who found spectral slopes different from the R-J slope $\alpha = 2$ in HST observations of five XTINSs (including J2143) in two spectral bands. A hint of nonthermal emission was also mentioned by D. L. Kaplan et al. (2003) in connection with the optical–UV spectrum of the peculiar XTINS RX J0720.4–3125, but other interpretations were not ruled out because of lack of deep (N) IR observations. Finally, the flux densities of J0806, measured by K+11 in the F140LP and F475W bands and B. Posselt et al. (2018) in the F160W band, are consistent with the spectrum being the sum of thermal and PL components, but it is hard to separate contributions to the NIR flux of the point source and the detected small-scale extended emission. Thus, the presence of the UVOIR PL component in other XTINSs is currently unclear.

Regarding the nonthermal X-ray component, the only XTINS from which it has apparently been detected is the brightest, J1856,[11] which has been extensively studied with several X-ray observatories. D. De Grandis et al. (2022) collected 1.43 Ms of clean XMM-Newton and NICER data, fit the X-ray spectrum with a 2BB+PL model, and found the PL component with a photon index $\Gamma = 1.4^{+0.5}_{-0.4}$ (i.e., $\alpha = -0.4^{+0.4}_{-0.6}$), dominating at $E \gtrsim 1.5$ keV. The 2–8 keV flux of this component corresponds to the efficiency $\eta_{2-8\,\rm keV} \sim 10^{-3}$. If we assume a similar X-ray efficiency for J2143, then its nonthermal flux would be $F_{2-8\,\rm keV} \sim 2.5 \times 10^{-16}\eta_{-3}d_{260}^{-2}$ erg cm^{-2} s^{-1}. This is below the constraint for the 4–8 keV flux obtained by C. Dessert et al. (2020). For $\alpha = -0.4$, it corresponds to $f_\nu \sim 3 \times 10^{-11}\eta_{-3}d_{260}^{-2}$ Jy and $\nu f_\nu \sim 0.8 \times 10^{-16}\eta_{-3}d_{260}^{-2}$ erg cm^{-2} s^{-1} at $E = 1$ keV. At $\eta_{-3} = 1$ and $d_{260} = 1$, these values are below the frames of Figures 6 and 7; i.e., such a nonthermal component is hardly detectable not only from J2143 but also from other XTINSs. It means that J1856 remains the only XTINS so far for which connection of the UVOIR and X-ray nonthermal emission can be studied, but there have been no deep observations of this object at $\lambda \gtrsim 6000$ Å.

4.2. Thermal Emission

Fitting the UVOIR spectrum of J2143 with the PL + BB model (see Equation (6) and Figure 3), we estimated the brightness temperature in the UV range, $kT_{\rm uv} \sim$ (15–25)$(d_{260}/R_{10})^2$ eV, where R_{10} is an equivalent sphere radius in the UV range, $R_{\rm uv}$, in units of 10 km. Note that even if the UV emission emerges from a uniformly heated NS surface, $R_{\rm uv}$ can be different from the NS radius because thermal emission may differ from the pure BB emission, $B_\nu(T) \to \varepsilon_\nu B_\nu(T)$ (with $\varepsilon_\nu \lesssim 1$), which corresponds to $R_{\rm uv} \sim \varepsilon_{\rm uv}^{1/2} R_{\rm NS}$, where $\varepsilon_{\rm uv}$ is a characteristic normalized emissivity in the UV range. Because the actual values of $\varepsilon_{\rm uv}R_{\rm NS}/d$ are unknown, we cannot reliably estimate the NS surface temperature from UVOIR observations alone.

The temperature can be better constrained if we include X-ray data in the analysis, which allows one to measure the (color) temperature and the R/d ratio separately. Fitting the X-ray spectrum with a BB model with one or two absorption features (1BB1G and 1BB2G models in Table 4), we find the color temperature $kT_{\rm hot} \approx 106$ eV and the equivalent sphere radius $R_{\rm hot} \approx 1.5 d_{260}$ km. Extrapolation of this model to the UV range gives a flux that is a factor of ~10 lower than observed; i.e., the multiwavelength thermal spectrum cannot be fitted with a single-temperature BB model, similar to other XTINSs. This apparent discrepancy can be caused by two factors: nonuniformity of NS surface temperature and the difference of the real thermal spectrum from the BB spectrum.

The temperature nonuniformity can be due to the anisotropic heat transfer from the hot NS interiors in the strong magnetic field of XTINSs (G. Greenstein & G. J. H.rtke 1983). The temperature distribution depends on the unknown geometry of the NS magnetic field (e.g., J. A. Pons et al. 2009), but at least for some geometries, the thermal emission spectrum can be approximated by a sum of two BB spectra (D. G. Yakovlev 2021). Such models have been used for spectral fits of XTINSs (e.g., T. M. Braje & R. W. Romani 2002; V. Burwitz et al. 2003) and RPPs (V. Abramkin et al. 2025 and references therein).

Applying this approach to the combined UVOIR and X-ray data, we fit the multiwavelength spectrum with the 2BB1G+PL and 2BB2G+PL models, assuming that the colder BB describes

[10] Note that the nonthermal UVOIR components of at least some RPPs are pulsed (O. Kargaltsev & G. Pavlov 2007), which likely excludes the PWN interpretation of the nonthermal component for those pulsars.

[11] For a second source, RX J0420.0–5022, there seems to be some excess that could be explained with either a BB or a PL component (T. Yoneyama et al. 2019; D. De Grandis et al. 2022).

both the soft X-ray and UV parts of the spectrum. The better fit with the 2BB2G+PL model yields $kT_{\rm cold} \approx 40$–50 eV, $R_{\rm cold} \sim 6d_{260}$ km, and $L_{\rm cold} \sim 2 \times 10^{31} d_{260}^2$ erg s^{-1}. The estimated $kT_{\rm cold}$ is within the range of 40–70 eV found for these quantities for RPPs of similar ages (see Table 4 in V. Abramkin et al. 2025). It is slightly lower than $kT_{\rm uv} \approx 60$ eV, which we would obtain from the BB+PL fit of the UVOIR spectrum at $R_{\rm uv} = R_{\rm cold}$ (i.e., $R_{10} = 0.6d_{260}$) and $A_V = 0.12$ (see Figures 3 and 4). The reason for this is the additional contribution from the R-J tail of $\rm BB_{hot}$ in the F140LP band, ∼10% of the total flux in that band, comparable to the contribution of the PL component (see Figures 6 and 7). The radius $R_{\rm cold}$ is smaller than the expected NS radius unless the target is unrealistically distant, $d \sim 600$–700 pc; this suggests a reduced mean emissivity in the FUV through soft X-ray range and a surface emission spectrum different from the pure BB. The bolometric luminosity of the $\rm BB_{cold}$ component is comparable to those of middle-aged RPPs that also have $R_{\rm cold}$ smaller than the expected NS radii.

Unlike middle-aged RPPs in which the $\rm BB_{hot}$ component usually dominates in the ∼0.5–1.5 keV band, for J2143, it dominates in the entire soft X-ray range, 0.2–2 keV, where the target was detected with XMM-Newton (see Figure 7). The ratio $T_{\rm hot}/T_{\rm cold} \approx 2.2$ is typical for middle-aged RPPs, but the ratio $R_{\rm hot}/R_{\rm cold} \sim 0.28$ is a factor of 3–7 larger than $R_{\rm hot}/R_{\rm cold} \sim 0.04$–$0.08$[12] for middle-aged RPPs. Contrary to middle-aged RPPs, the luminosity $L_{\rm hot} \sim 4 \times 10^{31} d_{260}^2$ erg s^{-1} exceeds $L_{\rm cold}$.

Moreover, $L_{\rm hot}$ exceeds the rotation energy loss rate, $\dot{E} = 2.0 \times 10^{30}$ erg s^{-1}, at any reasonable distances. It means that the hot region of J2143's surface is due to the anisotropic heat transfer rather than to the heating of the polar caps by relativistic particles precipitating from the magnetosphere.

We should not forget that the $\rm BB_{cold} + BB_{hot}$ model is a simplified description of thermal emission from an NS surface, whose true nature is not fully certain yet. For instance, some properties of the multiwavelength XTINS emission (such as the optical excess; see Section 1.1) could be explained by the presence of a gaseous hydrogen or helium atmosphere in the outer NS layers (G. G. Pavlov et al. 1996). However, the available models of at least optically thick light-element atmospheres cannot explain all the observed properties of XTINSs and middle-aged RPPs. Even if a fit is statistically acceptable, it requires an unrealistically large *R/d* ratio and/or a magnetic field inconsistent with other estimates, and it does not explain the observed X-ray absorption features (e.g., P. Arumugasamy et al. 2018; C. Malacaria et al. 2019; A. Vahdat et al. 2024; V. Abramkin et al. 2025). Models of an optically thin hydrogen atmosphere above the solid NS surface can explain the multiwavelength spectra of some XTINSs (W. C. G. Ho et al. 2007), but they require a narrow range of atmosphere thickness, i.e., a fine-tuning of model parameters.

A more viable hypothesis is that the surfaces of NSs with high magnetic fields are in a condensed (solid or liquid) state at the relatively low temperatures of XTINSs and not-too-young RPPs (e.g., Z. Medin & D. Lai 2007), likely with a nonuniform surface temperature distribution. Thermal X-ray spectra, emitted by condensed NS surfaces, resemble BBs with a reduced local emissivity (e.g., J. F. Pérez-Azorín et al. 2005, 2006). In the X-ray range, the frequency dependence of the local emissivity is rather complicated, with broad absorption features whose central frequencies and widths depend on the direction and magnitude of the local magnetic field. These features are strongly smoothed by the surface magnetic field nonuniformity and NS rotation, so that the X-ray spectrum resembles a Planck spectrum with a reduced emissivity, $f_\nu^{\rm unabs} \sim \pi (R_{\rm NS}/d)^2 \varepsilon_{\rm X} B_\nu(T)$; i.e., the apparent radius is $\sim \varepsilon_{\rm X}^{1/2} R_{\rm NS}$, $\varepsilon_{\rm X} < 1$. Our assumption in the 2BBnG fits that the same radius $R_{\rm cold}$ is associated with both the X-ray and UV parts of the spectrum implies $\varepsilon_{\rm X} \approx \varepsilon_{\rm uv}$. Such a relationship holds for the free-ions model of the condensed surface, while $\varepsilon_{\rm uv} \ll \varepsilon_{\rm X}$ for the fixed-ions model (M. van Adelsberg et al. 2005). The absorption spectral features at 0.74 keV and (perhaps) 0.4 keV could be related to the two depressions in the condensed surface spectrum, whose positions depend on the magnetic field as well as the density and chemical composition of the condensed matter.

The above discussion is based on phase-integrated spectra of the thermal component. More information, particularly about the temperature distribution over the NS surface, can be obtained from the X-ray pulse profile and phase-resolved spectroscopy. We defer this analysis to future work, which should include the previous XMM-Newton, NICER, and eROSITA datasets and use realistic models for the energy-dependent angular distributions and direction-dependent spectra for the condensed surface emission. Here we only mention that the three-peak structure of the 0.15–2 keV pulse profile, shown in Figure 5, is not consistent with models of internal surface heating in an NS with a centered dipole magnetic field (e.g., U. Geppert et al. 2006 and references therein). The relatively low pulsed fraction of ≈4% (which is, however, higher than ≈1.2% for J1856) could be associated, for instance, with J2143's spin axis being close to the line of sight, but the viewing angle can hardly be estimated without a detailed modeling.

4.3. Extended Emission

The characteristic size of ∼2″ of the putative extended emission from J2143, detected in the two NIR filters, corresponds to $\sim 0.8 \times 10^{16} d_{260}$ cm. The flux densities $f_\nu^{\rm ext} = 1.69 \pm 0.25$ and 0.88 ± 0.17 μJy in the F160W and F110W filters, respectively, are a factor of ∼10 larger than those of the compact object. They are consistent with a PL spectrum with the slope $\alpha^{\rm ext} = -2.23 \pm 0.83$, substantially steeper than the nonthermal NIR–optical emission of the pulsar. The flux in the 1–2 μm band can be estimated as $F_{1-2\,\mu{\rm m}}^{\rm ext} \approx 2.1 \times 10^{-15}$ erg cm^{-2} s^{-1}, which corresponds to the luminosity $L_{1-2\,\mu{\rm m}}^{\rm ext} \approx 1.7 \times 10^{28} d_{260}^2$ erg s^{-1}. If this emission is powered by the rotation energy loss of the pulsar, such luminosity corresponds to a very high NIR efficiency, $\eta_{1-2\,\mu{\rm m}}^{\rm ext} \equiv L_{1-2\,\mu{\rm m}}^{\rm ext}/\dot{E} \approx 8.6 \times 10^{-3} d_{260}^2$.

Putative extended NIR emission has been detected from only one other XTINS, J0806, with a size of ∼0.″8 (B. Posselt et al. 2018). Its flux density in F160W, the only HST NIR band in which it has been observed, was estimated as $f_\nu^{\rm ext} \sim 0.2$–0.4 μJy. The F160W flux, $F_{\rm F160W}^{\rm ext} \sim (4$–$8) \times 10^{-16}$ erg cm^{-2} s^{-1}, corresponds to the luminosity $L_{\rm F160W}^{\rm ext} \sim (3$–$6) \times 10^{27} d_{250}^2$ erg s^{-1}. With $\dot{E} = 2.6 \times 10^{29}$ erg s^{-1} (B. Posselt et al. 2024), the J0806 efficiency in this filter is $\eta_{\rm F160W}^{\rm ext} = (1.2$–$2.3) \times 10^{-2} d_{250}^2$. Thus, if J2143's extended emission is real, we see that the properties of the extended NIR emission are similar in these two XTINSs, which hints at a similar origin.

[12] Here we exclude Geminga from the set of middle-aged RPPs because the parameters of its faint hot component are very uncertain.

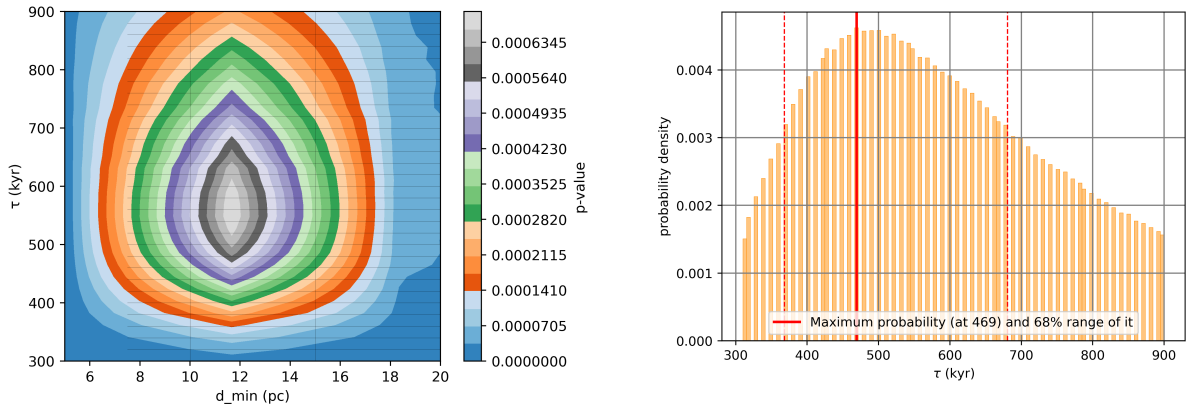

Figure 8. β Pic–Cap stellar association as a possible birthplace of J2143. The left panel shows the contours of the probability distribution for the encounter of J2143's trajectory with the stellar association; $d_{\rm min}$ is the smallest distance between the NS trajectory and the "center" of the association, and τ is the time interval between the closest encounter and the modern epoch. The p-values at the color bar reflect the combined probability for the set of simulation input parameters (see N. Tetzlaff et al. 2010b for details). The image for the contour plot has bin sizes of 5 pc in $d_{\rm min}$ and 20 kyr inτ. The right panel shows the age distribution of the simulation sample from the left panel in a 1D histogram. The highest probability for an encounter between J2143 and β Pic–Cap is at ∼470 kyr.

Possible interpretations of such extended NIR emission—a NIR-only PWN or a resolved disk around the NS—are discussed in detail by B. Posselt et al. (2018). Of these two interpretations, the former looks more plausible because of the large size of the extended structure. However, in the case of J2143, the putative extended emission is projected onto a crowded region, which strongly hampers the data analysis. Both J2143 and J0806 were also detected in the far-infrared at 160 μm with the Herschel Space Telescope, but for J2143, the peak of the 160 μm is further away from the pulsar position, and there are several other nearby far-infrared sources (B. Posselt et al. 2014). It should also be noted that the extinction in the directions of both XTINSs shows a steep steplike increase. If the two XTINSs are both in a region of increased interstellar particle density, that could explain the nondetection of these PWNe outside the NIR range.

4.4. Inferences from the Measured Proper Motion

The transverse velocity of J2143, $v_\perp = 7.1 \pm 0.7 d_{260}\,{\rm km\,s^{-1}}$, is one of the lowest measured for pulsars.[13] Considering typical NS velocities (G. Hobbs et al. 2005; F. Verbunt et al. 2017), it is likely that the radial velocity is much higher. Following the same approach as N. Tetzlaff et al. (2010b), we simulate 2 million different past trajectories of the pulsar in the Galactic potential to check for a possible origin of J2143 in a young stellar association.[14] For this, we assume a present distance of 260 pc and use probability distributions for the proper motions, radial velocity, etc., similar to that described by N. Tetzlaff et al. (2010b). At the characteristic age of the pulsar (∼3–4 Myr), the probability of an overlap between the NS trajectory and any track of the 140 young star associations is very low. Instead, the most probable and closest encounters between the NS and stellar associations took place less than 1 Myr ago. This is in line with other XTINSs, whose kinetic ages are much smaller than the characteristic ages. The β Pic–Cap stellar association (assumed size of 113 pc and age of 8 −34 Myr; N. Tetzlaff et al. 2010b) has the highest probability of possible trajectories crossing, at a smallest separation of ∼14 pc from the β Pic–Cap center ∼470 kyr ago (see Figure 8). Such a trajectory of J2143 would imply a today's radial velocity of 360 km s^{-1}, with J2143 moving away from us. If the very close β Pic–Cap is indeed the birthplace of J2143, the XTINS's birth supernova happened relatively close (∼70 pc) to the Sun.

5. Conclusions

1. The broadband UVOIR spectrum of J2143, obtained from our HST observations in five spectral bands, is dominated by a thermal (R-J) component in UV and a PL-like component at NIR–optical wavelengths, similar to the UVOIR spectra of middle-aged RPPs.
2. The flux density of the NIR–optical component, corrected for the interstellar absorption with a plausible V-band extinction coefficient $A_V = 0.12$, can be described by a PL model, $f_\nu^{\rm nonth} = f_0 (\nu/\nu_0)^\alpha$, with the slope $\alpha \sim -0.8$ and normalization $f_0 \sim 45$ nJy at $\nu_0 = 10^{15}$ Hz. The luminosity of this component in the UVOIR range is $L_1^{\rm nonth} - 10\,{\rm eV} \sim 7 \times 10^{27}\,{\rm erg\,s^{-1}}$ at the likely distance $d = 260$ pc, estimated from 3D extinction models and X-ray absorption. If powered by the pulsar's rotation energy loss, this luminosity corresponds to a very high efficiency of converting the spin-down power to UVOIR radiation: $\eta_1 - 10\,{\rm eV} \sim 4 \times 10^{-3}$.
3. The thermal UV component, $f_\nu^{\rm therm} \propto \nu^2$, is an R-J tail of a Planck-like thermal spectrum. The UVOIR observations provide an estimate of brightness temperature, $kT_{\rm uv} \sim 20 d_{260}^2 (R_{\rm uv}/10\,{\rm km})^{-2}\,{\rm eV}$, that is rather uncertain because of the unknown effective size of the UV-emitting region. The temperature is better constrained from the joint analysis of the UVOIR + X-ray spectrum, which can be fitted with the sum ${\rm BB_{hot}} + {\rm BB_{cold}}$, with $kT_{\rm hot} \sim 106$ eV, $R_{\rm hot} \sim 1.5 d_{260}$ km, $L_{\rm hot} \sim 4 \times 10^{31} d_{260}^2$ and $kT_{\rm cold} \sim 45$ eV, $R_{\rm cold} \sim 6 d_{260}$ km, $L_{\rm cold} \sim 2 \times 10^{31} d_{260}^2\,{\rm erg\,s^{-1}}$. Both the "hot" and "cold" bolometric luminosities exceed the spin-down power $\dot{E} = 2.0 \times 10^{30}\,{\rm erg\,s^{-1}}$, which supports the common assumption for XTINSs that the thermal emission is due to internal heating mechanisms rather

[13] Formally, it is the eighth lowest in the ATNF pulsar catalog, v2.6.5, but the transverse velocity values depend on the often poorly constrained distances.
[14] We used the list of young stellar associations compiled by N. Tetzlaff et al. (2010a)

than external heating by (magnetospheric) relativistic particles.

4. The images in the two NIR bands show hints of extended emission, with a $\sim 2''$ size and flux densities $f_\nu^{\rm ext} \sim 1.7$ and $0.9\,\mu$Jy at $\lambda = 1.54$ and $1.15\,\mu$m, respectively. They correspond to the NIR luminosity $L_{1-2\,\mu{\rm m}}^{\rm ext} \sim 2 \times 10^{28} d_{260}^2\,{\rm erg\,s^{-1}}$. If confirmed, the extended emission can be a peculiar infrared PWN with a very high efficiency, $\eta_{1-2\,\mu{\rm m}} \sim 0.01 d_{260}^2$, perhaps similar to the extended emission around J0806.
5. The measured proper motion of J2143, $\mu \sim 6\,{\rm mas\,yr^{-1}}$, corresponds to a low transverse velocity, $v_\perp \sim 7 d_{260}\,{\rm km\,s^{-1}}$). This XTINS could have been born $\sim$0.5 Myr ago very close to the Sun, in the stellar association β Pic–Cap. Similar to the the other XTINSs for which a "kinematic age" has been estimated, J2143 seems to be substantially younger than its characteristic age of 3.6 Myr.
6. Our spectral and timing analyses of the X-ray emission, obtained in a contemporaneous observation with the XMM-Newton Observatory, did not show significant differences with previous XMM-Newton and NICER observations of J2143.
7. We suggest that other XTINSs have similar UVOIR spectra, comprised of thermal and PL components, dominating in the UV and optical–IR ranges, respectively. This could be confirmed by more comprehensive UVOIR observations of these objects.
8. The UVOIR + X-ray spectrum of J2143 shows many properties similar to those of RPPs of comparable ages. The differences between these two types of objects could be due to the higher magnetic fields of newborn XTINSs, which led to additional heating, faster slowdown at their young ages, longer periods, and a shift of the nonthermal spectrum to lower photon energies.

Acknowledgments

We appreciate the help by Oleg Kargaltsev in the preparation of the observation proposal and the useful advice by Jay Anderson on the observational setup for the NIR observations. We thank Norbert Schartel for granting the TOO XMM-Newton observation contemporaneous with the HST observation. We are indebted to Yura Shibanov for sharing the results of the spectral analysis of previous X-ray observations of J2143. We especially thank Rosine Lallement and Gordian Edenhofer for helpful discussions and providing extinction maps in the direction toward J2143, which allowed us to obtain a reliable estimate for the distance to this object and the corresponding extinction. We warmly thank Nina Tetzlaff, Kieran Moore, and Arnas Matulaitis for their help with the birthplace simulation code.

Support for program #17476 was provided by NASA through a grant from the Space Telescope Science Institute, which is operated by the Association of Universities for Research in Astronomy, Inc., under NASA contract NAS 5-26555. Some of the data presented in this paper were obtained from the Mikulski Archive for Space Telescopes (MAST) at the Space Telescope Science Institute.

This research has used data, tools, or materials developed as part of the EXPLORE project that has received funding from the European Union's Horizon 2020 research and innovation program under grant agreement No. 101004214. This work has made use of data from the European Space Agency (ESA) mission Gaia (https://www.cosmos.esa.int/gaia), processed by the Gaia Data Processing and Analysis Consortium (DPAC; https://www.cosmos.esa.int/web/gaia/dpac/consortium). Funding for the DPAC has been provided by national institutions, in particular the institutions participating in the Gaia Multilateral Agreement.

The HST data presented in this article were obtained from the Mikulski Archive for Space Telescopes (MAST) at the Space Telescope Science Institute. The specific observations analyzed can be accessed via doi:10.17909/9jev-5m35.

Facilities: HST (ACS/SBC, ACS/WFC, WFC3/UVIS, WFC3/IR) and XMM (EPIC).

Software: XSPEC (K. A. Arnaud 1996), XMM SAS (C. Gabriel et al. 2004), Graphical Astronomy and Image Analysis Tool (M. J. Currie et al. 2014), G-Tomo (R. Lallement et al. 2022), Astropy (Astropy Collaboration et al. 2022), Matplotlib (J. D. Hunter 2007).

Appendix
The Flux in the Region around the Neutron Star

We noticed some possible flux enhancement around the target in the F160W image. It seems most prominent in an area with distance up to $2''$ from J2143. As the region is very crowded, there is the possibility of very faint background sources in that area. Aiming to avoid such potential background sources, we define a polygon aperture (area of $\approx 13''^2$) around the NS; see Figure 9. We use the same polygon shape for 26 background apertures that allow us to measure the background flux and its error. We then use the same procedure as in Section 3.1.1, Equation (1), to determine the net flux density in the polygon region, $f_{\rm F160W}^{\rm ext} = 1.69 \pm 0.25\,\mu$Jy. We use the same source aperture and procedure to measure the flux density in the F110W band, $f_{\rm F110W}^{\rm ext} = 0.88 \pm 0.17\,\mu$Jy.

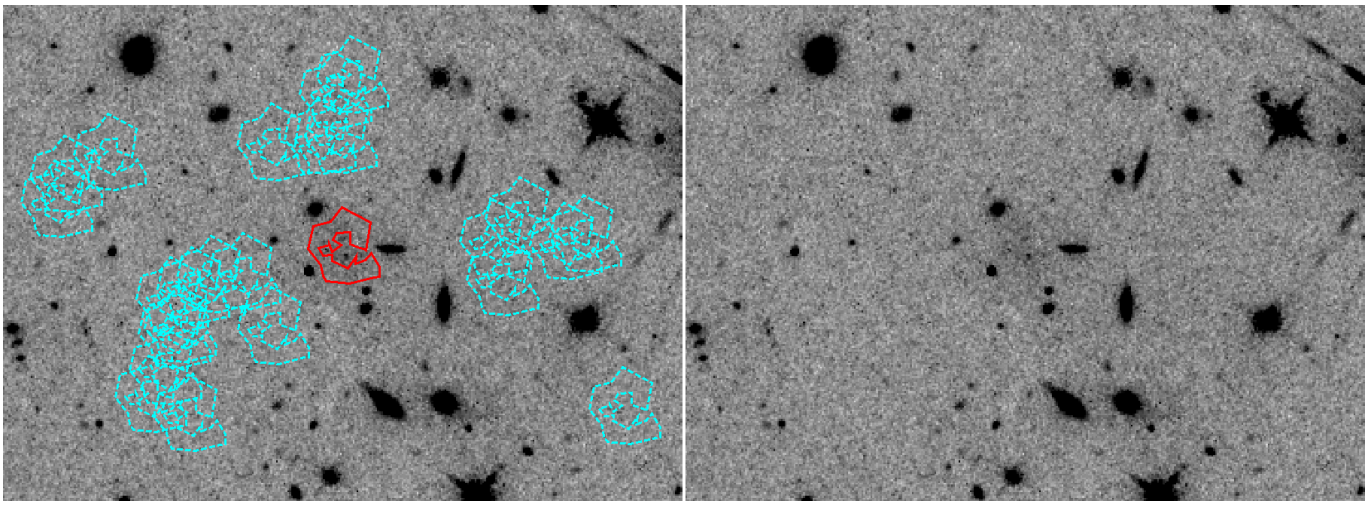

Figure 9. The polygon apertures in the F160W image that were used to measure the apparent flux enhancement in the region around the NS (red). The 26 background apertures with the same shape are marked with cyan dashed regions. The right panel shows the same image (about $46'' \times 33''$, north is up, east is left) to allow an undisturbed view. For a zoom-in of the source region, see Figure 1.

ORCID iDs

George G. Pavlov https://orcid.org/0000-0002-7481-5259
Vadim Abramkin https://orcid.org/0000-0002-9892-7546
B. Posselt https://orcid.org/0000-0003-2317-9747

References

Abramkin, V., Pavlov, G. G., Shibanov, Y., Posselt, B., & Kargaltsev, O. 2025, A&A, 696, A121
Arnaud, K. A. 1996, ASPC, 101, 17
Arumugasamy, P., Kargaltsev, O., Posselt, B., Pavlov, G. G., & Hare, J. 2018, ApJ, 869, 97
Astropy Collaboration, Price-Whelan, A. M., Lim, P. L., et al. 2022, ApJ, 935, 167
Avila, R. J., Bohlin, R., Hathi, N., et al. 2019, Instrument Science Report ACS 2019-5, Space Telescope Science Institute
Bogdanov, S., & Ho, W. C. G. 2024, ApJ, 969, 53
Braje, T. M., & Romani, R. W. 2002, ApJ, 580, 1043
Burwitz, V., Haberl, F., Neuhäuser, R., et al. 2003, A&A, 399, 1109
Cropper, M., Zane, S., Turolla, R., et al. 2007, Ap&SS, 308, 161
Currie, M. J., Berry, D. S., Jenness, T., et al. 2014, ASPC, 485, 391
De Grandis, D., Rigoselli, M., Mereghetti, S., et al. 2022, MNRAS, 516, 4932
Dessert, C., Foster, J. W., & Safdi, B. R. 2020, ApJ, 904, 42
Edenhofer, G., Zucker, C., Frank, P., et al. 2024, A&A, 685, A82
Ertan, Ü., Çalışkan, Ş., & Alpar, M. A. 2017, MNRAS, 470, 1253
Foight, D. R., Güver, T., Özel, F., & Slane, P. O. 2016, ApJ, 826, 66
Fruchter, A. S., et al. 2010, in 2010 Space Telescope Science Institute Calibration Workshop, ed. S. Deustua & C. Oliveira (Space Telescope Science Institute), 382
Gabriel, C., Denby, M., Fyfe, D. J., et al. 2004, ASPC, 314, 759
Gaia Collaboration, Prusti, T., de Bruijne, J., H., J., et al. 2016, A&A, 595, A1
Gaia Collaboration, Vallenari, A., Brown, A. G. A., et al. 2023, A&A, 674, A1
Geppert, U., Küker, M., & Page, D. 2006, A&A, 457, 937
Gonzaga, S., et al. 2012, The DrizzlePac Handbook ads (Space Telescope Science Institute)
Gordon, K. D., Clayton, G. C., Decleir, M., et al. 2023, ApJ, 950, 86
Green, G. M., Schlafly, E., Zucker, C., Speagle, J. S., & Finkbeiner, D. 2019, ApJ, 887, 93
Greenstein, G., & Hartke, G. J. 1983, ApJ, 271, 283
Haberl, F. 2007, Ap&SS, 308, 181
Haberl, F., Turolla, R., de Vries, C. P., et al. 2006, A&A, 451, L17
Hare, J., Pavlov, G. G., Posselt, B., et al. 2024, ApJ, 972, 176
Hare, J., Volkov, I., Pavlov, G. G., Kargaltsev, O., & Johnston, S. 2021, ApJ, 923, 249
Ho, W. C. G., Kaplan, D. L., Chang, P., van Adelsberg, M., & Potekhin, A. Y. 2007, MNRAS, 375, 821
Hobbs, G., Lorimer, D. R., Lyne, A. G., & Kramer, M. 2005, MNRAS, 360, 974
Hohle, M. M., Haberl, F., Vink, J., et al. 2012, MNRAS, 423, 1194
Hunter, J. D. 2007, CSE, 9, 90
Kaplan, D. L., Kamble, A., van Kerkwijk, M. H., & Ho, W. C. G. 2011, ApJ, 736, 117
Kaplan, D. L., & van Kerkwijk, M. H. 2009a, ApJ, 705, 798
Kaplan, D. L., & van Kerkwijk, M. H. 2009b, ApJL, 692, L62
Kaplan, D. L., van Kerkwijk, M. H., Marshall, H. L., et al. 2003, ApJ, 590, 1008
Kargaltsev, O., & Pavlov, G. 2007, Ap&SS, 308, 287
Kondratiev, V. I., McLaughlin, M. A., Lorimer, D. R., et al. 2009, ApJ, 702, 692
Kurpas, J., Schwope, A. D., Pires, A. M., & Haberl, F. 2024, A&A, 683, A164
Lallement, R., Vergely, J. L., Babusiaux, C., & Cox, N. L. J. 2022, A&A, 661, A147
Leike, R. H., Glatzle, M., & Enßlin, T. A. 2020, A&A, 639, A138
Malacaria, C., Bogdanov, S., Ho, W. C. G., et al. 2019, ApJ, 880, 74
Mancini Pires, A., Schwope, A., & Kurpas, J. 2023, IAUS, 363, 288
Medin, Z., & Lai, D. 2007, MNRAS, 382, 1833
Pavlov, G. G., Posselt, B., & Kargaltsev, O. Y. 2023, HST Proposal. Cycle 31, ID. #17476,
Pavlov, G. G., Welty, A. D., & Córdova, F. A. 1997, ApJL, 489, L75
Pavlov, G. G., Zavlin, V. E., Truemper, J., & Neuhaeuser, R. 1996, ApJL, 472, L33
Pérez-Azorín, J. F., Miralles, J. A., & Pons, J. A. 2005, A&A, 433, 275
Pérez-Azorín, J. F., Miralles, J. A., & Pons, J. A. 2006, A&A, 451, 1009
Pires, A. M., Motch, C., Kurpas, J., et al. 2022, A&A, 666, A148
Pires, A. M., Schwope, A. D., Haberl, F., et al. 2019, A&A, 623, A73
Pons, J. A., Miralles, J. A., & Geppert, U. 2009, A&A, 496, 207
Posselt, B., Arumugasamy, P., Pavlov, G. G., et al. 2012, ApJ, 761, 117
Posselt, B., Karastergiou, A., Johnston, S., et al. 2023, MNRAS, 520, 4582
Posselt, B., Neuhäuser, R., & Haberl, F. 2009, A&A, 496, 533
Posselt, B., Pavlov, G. G., Ertan, Ü., et al. 2018, ApJ, 865, 1
Posselt, B., Pavlov, G. G., Ho, W. C. G., & Haberl, F. 2024, ApJ, 972, 197
Posselt, B., Pavlov, G. G., Popov, S., & Wachter, S. 2014, ApJS, 215, 3
Posselt, B., Popov, S. B., Haberl, F., et al. 2008, A&A, 482, 617
Reid, M. J., Schneps, M. H., Moran, J. M., et al. 1988, ApJ, 330, 809
Rodrigo, C., Solano, E., & Bayo, A., 2012 IVOA Working Draft, doi:10.5479/ADS/bib/2012ivoa.rept.1015R
Schwope, A. D., Erben, T., Kohnert, J., et al. 2009, A&A, 499, 267
Skelton, R. E., Whitaker, K. E., Momcheva, I. G., et al. 2014, ApJS, 214, 24
Tetzlaff, N., Neuhaeuser, R., Hohle, M. M., & Maciejewski, G. 2010a, yCat, J/MNRAS/402/2369
Tetzlaff, N., Neuhäuser, R., Hohle, M. M., & Maciejewski, G. 2010b, MNRAS, 402, 2369
Vahdat, A., Posselt, B., Pavlov, G. G., et al. 2024, ApJ, 963, 138
van Adelsberg, M., Lai, D., Potekhin, A. Y., & Arras, P. 2005, ApJ, 628, 902

van Kerkwijk, M. H., Kaplan, D. L., Pavlov, G. G., & Mori, K. 2007, ApJL, 659, L149
van Kerkwijk, M. H., & Kulkarni, S. R. 2001, A&A, 380, 221
Verbunt, F., Igoshev, A., & Cator, E. 2017, A&A, 608, A57
Vergely, J. L., Lallement, R., & Cox, N. L. J. 2022, A&A, 664, A174
Wilms, J., Allen, A., & McCray, R. 2000, ApJ, 542, 914
Yakovlev, D. G. 2021, MNRAS, 506, 4593
Yoneyama, T., Hayashida, K., Nakajima, H., & Matsumoto, H. 2019, PASJ, 71, 17
Zampieri, L., Campana, S., Turolla, R., et al. 2001, A&A, 378, L5
Zane, S., Cropper, M., Turolla, R., et al. 2005, ApJ, 627, 397
Zane, S., Mignani, R. P., Turolla, R., et al. 2008, ApJ, 682, 487